Atmos. Meas. Tech., 14, 5319–5332, 2021
https://doi.org/10.5194/amt-14-5319-2021

Atmospheric Measurement Techniques
Open Access
EGU

Iodide CIMS and m/z 62: the detection of HNO_3 as NO_3^- in the presence of PAN, peroxyacetic acid and ozone

Raphael Dörich, Philipp Eger, Jos Lelieveld, and John N. Crowley

Atmospheric Chemistry Department, Max Planck Institute for Chemistry, 55128, Mainz, Germany

Correspondence: John N. Crowley (john.crowley@mpic.de)

Received: 1 March 2021 – Discussion started: 18 March 2021
Revised: 14 May 2021 – Accepted: 16 June 2021 – Published: 3 August 2021

Abstract. Chemical ionisation mass spectrometry (CIMS) using I^- (the iodide anion), hereafter I-CIMS, as a primary reactant ion has previously been used to measure NO_3 and N_2O_5 both in laboratory and field experiments. We show that reports of large daytime mixing ratios of NO_3 and N_2O_5 (both usually present in detectable amounts only at night) are likely to be heavily biased by the ubiquitous presence of HNO_3 in the troposphere and lower stratosphere. We demonstrate in a series of laboratory experiments that the CIMS detection of HNO_3 at m/z 62 using I^- ions is efficient in the presence of peroxy acetyl nitric anhydride (PAN) or peroxyacetic acid (PAA) and especially O_3. We have characterised the dependence of the sensitivity to HNO_3 detection on the presence of acetate anions ($CH_3CO_2^-$, m/z 59, from either PAN or PAA). The loss of $CH_3CO_2^-$ via conversion to NO_3^- in the presence of HNO_3 may represent a significant bias in I-CIMS measurements of PAN and PAA in which continuous calibration (e.g. via addition of isotopically labelled PAN) is not carried out. The greatest sensitivity to HNO_3 at m/z 62 is achieved in the presence of ambient levels of O_3 whereby the thermodynamically disfavoured, direct reaction of I^- with HNO_3 to form NO_3^- is bypassed by the formation of IO_x^-, which reacts with HNO_3 to form, for example, iodic acid and NO_3^-. The ozone and humidity dependence of the detection of HNO_3 at m/z 62 was characterised in laboratory experiments and applied to daytime, airborne measurements in which good agreement with measurements of the $I^-(HNO_3)$ cluster ion (specific for HNO_3 detection) was obtained. At high ozone mixing ratios, we show that the concentration of I^- ions in our ion–molecule reactor (IMR) is significantly depleted. This is not reflected by changes in the measured I^- signal at m/z 127 as the IO_x^- formed does not survive passage through the instrument but is likely detected after fragmentation to I^-. This may result in a bias in measurements of trace gases using I-CIMS in stratospheric air masses unless a calibration gas is continuously added or the impact of O_3 on sensitivity is characterised.

1 Introduction

The use of iodide anions (I^-) as primary ions in mass-spectrometric studies of ion–molecule reactions has a long history. Fehsenfeld et al. (1975) and Davidson et al. (1978) established that the nitrate anion (NO_3^-, m/z 62) was formed in a rapid reaction between I^- and N_2O_5. NO_3^- was also identified as the main product of the reaction between I^- and $ClONO_2$ (Huey et al., 1995). The large rate constants for reaction of I^- with N_2O_5 and $ClONO_2$ led to the development of chemical ionisation mass spectrometry (CIMS) using I^- primary ions (henceforth I-CIMS) in kinetic studies of heterogeneous, atmospheric reactions (e.g. Hanson and Ravishankara, 1991) and more recently I-CIMS has found widespread deployment for measurement of atmospheric trace gases (Huey, 2007, and references therein). Early field measurements utilised I-CIMS to detect N_2O_5 and peroxyacetyl nitric anhydride (PAN, $CH_3C(O)O_2NO_2$) (Slusher et al., 2004), but since then the range of molecules that have been detected using I^- has greatly increased and trace gases as diverse as inorganic radicals and halogenates and a host of organic species are now routinely measured (Huey, 2007; Lee et al., 2014; Iyer et al., 2017; Riva et al., 2019). In this work, we focus on the detection of two atmospherically important trace gases N_2O_5 and HNO_3 using a CIMS operating with I^- reactant ions.

Both N_2O_5 and HNO_3 are formed in the atmosphere by the sequential oxidation of NO, which has both anthropogenic and natural sources. In a well-known series of reactions (Lightfoot et al., 1992; Atkinson et al., 2004), NO is oxidised (Reactions R1 and R2) by reaction with O_3 or peroxyl radicals (RO_2) to NO_2, which during the day, may be removed by reaction with OH to form HNO_3 (Reaction R3) and during the night to form N_2O_5 (Reactions R4 and R5).

$$NO + O_3 \rightarrow NO_2 + O_2 \quad \text{(R1)}$$

$$NO + RO_2 \rightarrow NO_2 + O_2 \quad \text{(R2)}$$

$$NO_2 + OH + M \rightarrow HNO_3 + M \quad \text{(R3)}$$

$$NO_2 + O_3 \rightarrow NO_3 + O_2 \quad \text{(R4)}$$

$$NO_3 + NO_2 + M \rightarrow N_2O_5 + M \quad \text{(R5)}$$

Both HNO_3 and N_2O_5 have important, non-gas-phase loss processes (Crowley et al., 2010) such as uptake to particles and other surfaces. In addition, N_2O_5 can thermally dissociate back to NO_3.

The chain of reactions to form N_2O_5 is broken during the day as NO_3 is generally photolysed within a few seconds (Wayne et al., 1991) and also reacts with NO so that N_2O_5 is expected to be present at significant levels only at night-time.

The detection of N_2O_5 using I^- reactant ions can be achieved by monitoring either the NO_3^- product at m/z 62 (see above) or the adduct ion at m/z 235 (Kercher et al., 2009). The former is reported to be more sensitive and less dependent on water vapour concentrations but less specific, with large and highly variable background signals potentially arising from trace gases such as NO_3, $ClONO_2$ and $BrONO_2$. Despite this, night-time N_2O_5 has been monitored in ambient air (as NO_3^-) using I^- reactant ions, showing reasonable agreement with optical methods (Slusher et al., 2004; Dubé et al., 2006; Chang et al., 2011).

During a recent, airborne deployment of our I-CIMS, we monitored NO_3^- at m/z 62 in an attempt to detect N_2O_5 during two night-time flights. The air masses we investigated were mainly in the tropical free and upper troposphere and lower stratosphere, and we did not expect significant interference from, for example, halogen nitrates at m/z 62. However, our airborne measurements (described in detail in Sect. 4) revealed a large and variable signal at m/z 62 during both the day and night. To illustrate this, raw signals obtained during daytime when the aircraft sampled air masses with varying degrees of stratospheric influence are displayed in Fig. S1 in the Supplement. The signal at m/z 62 is large and highly variable and is not affected by addition of NO to the heated inlet, ruling out its assignment to either N_2O_5 or NO_3 (see below). The great increase in signal when entering the lower stratosphere and the obvious correlation with O_3 (Fischer et al., 1997; Popp et al., 2009) provided an early clue to the identity of the trace gas detected at m/z 62 which we initially assigned to HNO_3. Our results thus appeared to contrast the conclusions of a previous observation of a large daytime signal at m/z 62 when deploying an I-CIMS (in this case in the boundary layer), which was interpreted as resulting (at least in part) from high levels of daytime NO_3 and/or N_2O_5 (Wang et al., 2014). Based on complementary laboratory experiments, Wang et al. (2014) showed, in accord with earlier investigations (Fehsenfeld et al., 1975; Huey et al., 1995), that HNO_3 is not detected sensitively at m/z 62 using I-CIMS.

The unexpected observation of a large daytime signal at m/z 62 during airborne operation led us to perform a series of laboratory experiments to identify potential "interfering" trace gases at this mass-to-charge ratio when using I-CIMS. In contrast to the conclusions drawn from previous studies, our laboratory and airborne measurements show that, during daytime, the predominant contributor to m/z 62 when sampling ambient air (in the presence of ozone) is likely to be HNO_3.

2 Experimental details

The I-CIMS we used in our laboratory and airborne investigations (see Fig. 1) is similar to that described by Slusher et al. (2004) and Zheng et al. (2011) and was originally constructed in collaboration with Georgia Tech as a prototype instrument of the company THS (http://thsinstruments.com, last access: 30 July 2021). It is essentially a hybrid of the instruments described by Phillips et al. (2013) and Eger et al. (2019), the former using a ^{210}Po ion source, the latter an electrical discharge source but with improved (digital) control of the MS settings enabling different mass-to-charge ratios to be monitored using different potentials for the collisional dissociation of cluster ions. For all the experiments described below, the ^{210}Po ion source was used to generate I^- as this configuration has much better sensitivity for PAN, the main target trace gas during the deployment of the I-CIMS on the HALO aircraft (High Altitude Long range platform for atmospheric Observations). The set-up for PAN detection includes a heated inlet section ($\sim 170\,°C$, 100 mbar, residence time ~ 40 ms) to thermally dissociate PAN to $CH_3C(O)O_2$ which subsequently reacts with I^- to form the acetate anion ($CH_3CO_2^-$) which is detected at m/z 59. At this inlet temperature and pressure, the lifetime of PAN with respect to thermal decomposition < 3 ms (Ammann et al., 2021). For N_2O_5, the lifetime with respect to its thermal dissociation to NO_2 and NO_3 is ~ 0.5 ms (IUPAC, 2021) so that N_2O_5 is stoichiometrically converted to NO_3 and the instrument measures the sum of N_2O_5 and NO_3 at m/z 62. In order to separate PAN signals from those of peroxyacetic acid ($CH_3C(O)OOH$, also detected as $CH_3CO_2^-$ at m/z 59), we periodically add NO ($\sim 5 \times 10^{12}$ molecule cm^{-3}) to the inlet to remove $CH_3C(O)O_2$ and thus eliminate sensitivity to PAN. As NO reacts more rapidly with NO_3 than with $CH_3C(O)O_2$ at 170 °C ($k_{NO+NO_3} = 2.3 \times 10^{-11}$ cm^3 molecule^{-1} s^{-1}, $k_{NO+CH_3C(O)O_2} = 1.4 \times 10^{-11}$ cm^3 molecule^{-1} s^{-1}; IUPAC,

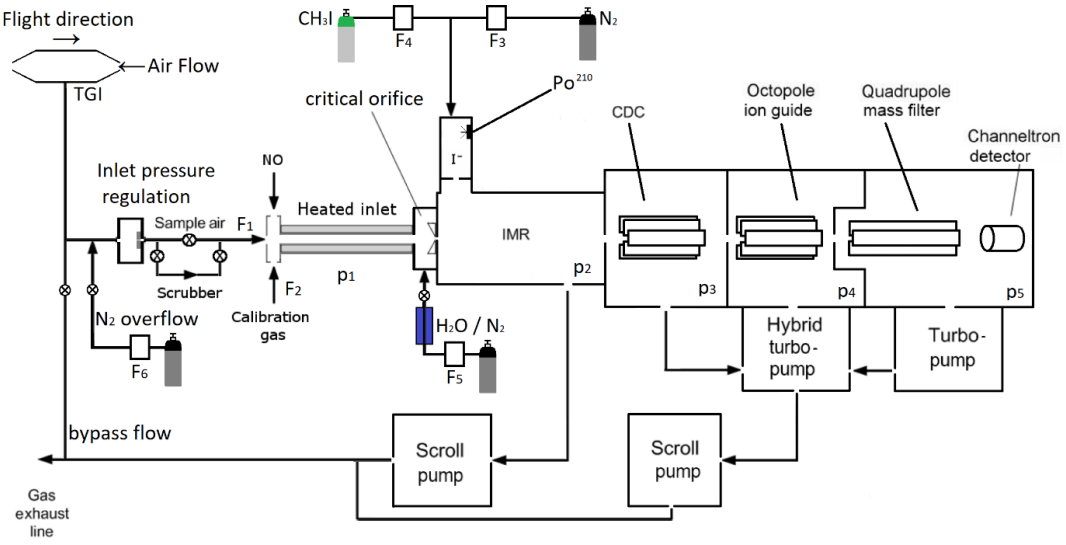

Figure 1. Schematic diagram illustrating the central components of the I-CIMS used in this work. IMR = ion–molecule reactor, CDC = collisional dissociation chamber, $F_1 = 1250\,\mathrm{cm^3\,(STP)\,min^{-1}}$, $F_2 = 50\,\mathrm{cm^3\,(STP)\,min^{-1}}$, $F_3 = 750\,\mathrm{cm^3\,(STP)\,min^{-1}}$, $F_4 = 4\,\mathrm{cm^3\,(STP)\,min^{-1}}$, $F_5 = 50\,\mathrm{cm^3\,(STP)\,min^{-1}}$. $p1 = 100$ mbar, $p2 = 24$ mbar, $p3 = 0.6$ mbar, $p4 = 6 \times 10^{-3}$ mbar, $p5 = 9 \times 10^{-5}$ mbar. The heated inlet is made of PFA tubing. TGI = Trace-gas inlet. When overflowing the inlet line, the valve to the exhaust line is closed. When sampling air, the valve to the N_2 bottle is closed.

2021), the concentration of NO added is also sufficient to quantitatively titrate NO_3 to NO_2 and thus provides a measure of the "background" signal at m/z 62 in the absence of NO_3 and N_2O_5.

During airborne operation on HALO, the dynamic pressure generated in a forward facing trace gas inlet (TGI) located on top of the aircraft (see Fig. 1) was used to create a flow of air through 1/4 in. (OD) PFA tubing sampling at an angle of 90° to the flight direction. The 1/4 in. tubing was attached to a 1/2 in. (OD) PFA tube attached to an exhaust plate at the underside of the aircraft to create a fast "bypass" flow. The bypass flow was sub-sampled (again at 90° and by 1/4 in. PFA tubing heated to 40 °C) by the 1.4 L (STP) $\mathrm{min^{-1}}$ flow into the I-CIMS. Sub-sampling twice at 90° to the flow was helpful in reducing the number of large particles (e.g. cloud droplets) that could enter the thermal dissociation inlet and IMR.

The thermal dissociation inlet of the I-CIMS is regulated to a pressure of 100 mbar, which results in a pressure in the ion–molecule reactor of 24 mbar. This way, a stable pressure in the thermal dissociation inlet and the ion–molecule reactor (IMR) was maintained at altitudes up to ∼ 15 km. Prior to take off, the inlet line and TGI were flushed with nitrogen to prevent contamination by the high levels of pollutant trace gases at the airport. As described in Eger et al. (2019) negative ions exiting the IMR were declustered in passage through a collisional dissociation region (CDC, 0.6 mbar) before passing through an octopole ion guide (6×10^{-3} mbar) and a quadrupole for mass selection (9×10^{-5} mbar) prior to detection using a channeltron.

I^- ions were generated by combining flows of $4\,\mathrm{cm^3\,(STP)\,min^{-1}}$ CH_3I/N_2 (400 ppmv) with $750\,\mathrm{cm^3\,(STP)\,min^{-1}}$ N_2 and passing the mixture through a 370 MBq ^{210}Po source. Under standard operating conditions (including airborne deployment), a constant amount of H_2O was added to the IMR by flowing $50\,\mathrm{cm^3\,(STP)\,min^{-1}}$ N_2 (at 1 bar pressure) through a 30 cm length of water-permeable 1/8 in. tubing (Permapure) immersed in water. The $50\,\mathrm{cm^3\,(STP)\,min^{-1}}$ flow of N_2 acquires a relative humidity close to 100 % in transit through the tubing and is subsequently mixed with the dry N_2 flow and sample air. Under these conditions, the ratio of signals at m/z 145 ($I^-(H_2O)$) to that at m/z 127 (I^-) was 0.068. By comparison with calibration curves (see Fig. S2 and associated text) this indicates an H_2O concentration in the IMR of $\sim 4 \times 10^{14}\,\mathrm{molecule\,cm^{-3}}$. For laboratory tests, the amount of water in the IMR could be increased by reducing the pressure in the permeable tube (thus increasing the mole fraction of H_2O) or set to zero by bypassing the humidifier.

Based on a (calculated) literature value for the free energy of formation of $I^-(H_2O)_1$ of $-6.1\,\mathrm{kcal\,mol^{-1}}$ (Teiwes et al., 2019), we derive an equilibrium constant (at 298 K) of $K_6 = 1.16 \times 10^{-15}\,\mathrm{cm^3\,molecule^{-1}}$ for the formation and thermal dissociation of $I^-(H_2O)_1$:

$$I^- + H_2O \rightleftharpoons I^-(H_2O)_1. \quad \text{(R6)}$$

With an H_2O concentration (in the IMR) of $3.9 \times 10^{14}\,\mathrm{molecule\,cm^{-3}}$, this implies that the ratio $[I^-(H_2O)_1]/[I^-] = 0.45$. Our measured ratio of signals at m/z 145 ($I^-(H_2O)$) : m/z 127 (I^-) was a factor ∼ 6 lower,

reflecting the fact that, even when the declustering potential is reduced to its minimum value, most $I^-(H_2O)$ ions do not survive the CDC region.

During extended operation of the CIMS, changes in sensitivity were captured by monitoring the primary ion signal (I^- and its water cluster). Background signals at each of the mass-to-charge ratios monitored were obtained by passing the sampled air through a tubular scrubber (aluminium) filled with stainless-steel wool heated to 120 °C.

3 Laboratory characterisation

3.1 Detection of HNO_3 at m/z 62: the role of ozone

As described above, our observations of a clear correlation between m/z 62 and O_3 mixing ratios during the first HALO deployment of the I-CIMS strongly suggested that HNO_3 was the origin of the signal although previous experiments had shown that I^- does not react with HNO_3 to form NO_3^-. In order to determine the sensitivity of our I-CIMS to HNO_3, we constructed a permeation source in which a 20 cm^3 (STP) min^{-1} flow of zero air was passed through a 1 m length of PFA tubing (0.125 in. OD) which was formed into a coil and submerged in an aqueous solution of 65 % HNO_3 held at 50 °C. The permeation rate was determined by passing the 20 cm^3 (STP) min^{-1} flow through an optical absorption cell and measuring the optical extinction at 185 nm where the absorption cross-section of HNO_3 is well known (Dulitz et al., 2018). For the I-CIMS calibration, the 20 cm^3 (STP) min^{-1} output was dynamically diluted to generate a mixing ratio of between 5 and 50 ppbv. Based on uncertainties in the absorption cross-section (5 %), the reproducibility of the optical measurement and the dilution factor, the uncertainty of the HNO_3 mixing ratio is estimated as 15 %.

Figure 2 shows the response of the I-CIMS at m/z 62 to addition of various amounts of HNO_3. Throughout the paper, when presenting raw data, we generally normalise the I-CIMS signal by dividing by the primary ion signal at m/z 127. This is standard practice and corrects for drifts in the CH_3I flow which may occur over several hours after the instrument was switched from standby mode to operational mode. It also accounts for longer-term drifts caused by the weakening activity of the ^{210}Po source over the duration of a measurement campaign (months) or since the last calibration and for loss of detector sensitivity over similar time periods. We show later that, when adding large concentrations of reactants that significantly deplete the primary ion signal at m/z 127, this procedure may lead to bias is some measurements. For this reason, when detecting HNO_3 at m/z 190 (see later), we normalise to an interpolated signal at m/z 127 that was measured when the air was scrubbed.

The weak signal in the absence of O_3 (blue data points) confirms the conclusions of previous studies that derive a low rate coefficient for Reaction (R7). For comparison, approximate, relative sensitivities to PAN (m/z 59), N_2O_5 (m/z 62) and HNO_3 (m/z 62), using this instrument are 1, 0.1 and 5×10^{-4}, respectively. Indeed, as written below, Reaction (R7) is endothermic by $\sim 43\,kJ\,mol^{-1}$ (Goos et al., 2005).

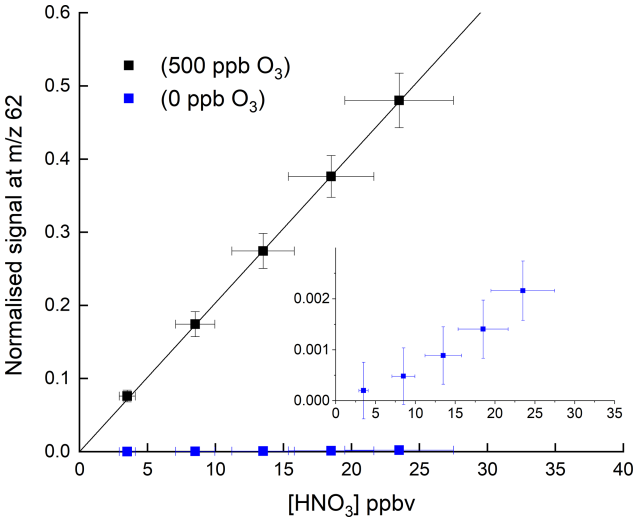

Figure 2. HNO_3 detection at m/z 62 in the absence and presence (500 ppbv) of O_3. The solid lines are non-weighted, linear regressions to the data and are 2.035×10^{-2} and 8.033×10^{-5} $ppbv^{-1}$ HNO_3 when 500 ppbv O_3 and zero O_3 were present, respectively. The inset (same x and y axes as in the full figure) is an expanded view of the signal obtained in the absence of O_3. The error bars represent 15 % systematic uncertainty in the HNO_3 concentration and 2σ statistical uncertainty in the signal at m/z 62.

$$I^- + HNO_3 \rightarrow NO_3^- + HI \quad \text{(R7)}$$

In a further series of experiments, we measured the response of the I-CIMS to HNO_3 when adding O_3 to the zero air. The results, also plotted in Fig. 2 (black symbols), indicate a factor ~ 250 increase in the signal at m/z 62 when ~ 500 ppbv ozone was added. There are two possible explanations for this observation. The first involves conversion of NO_2 impurity (which is present as a ~ 8 % impurity in the HNO_3 permeation flow) to NO_3 and N_2O_5 (Reactions R1, R4, and R5), which are subsequently detected. This can however be ruled out as the rate-limiting step in the formation of NO_3 is the slow reaction between NO_2 and O_3 with $k_4 = 3.5 \times 10^{-17}$ cm^3 $molecule^{-1}$ s^{-1} at room temperature (Atkinson et al., 2004). The addition of 1000 ppbv O_3 (equivalent to a concentration of 2.4×10^{13} molecule cm^{-3}) would only convert an insignificant fraction of the NO_2 to NO_3 in the ~ 40 ms reaction time available from the point of mixing to the IMR. This was confirmed by adding NO (7.7 ppm) to the inlet, which would remove any NO_3 (see above) and observing no change in the signal at m/z 62.

The second explanation is that the presence of O_3 results in the generation of further reagent ions that can react with HNO_3. Iodide anions are known to react with O_3, leading, in a series of exothermic reactions, to the formation of iodate (Williams et al., 2002; Teiwes et al., 2018; Bhujel et al., 2020).

$$I^- + O_3 \rightarrow IO^- + O_2 \quad \text{(R8)}$$
$$IO^- + O_3 \rightarrow IO_2^- + O_2 \quad \text{(R9)}$$
$$IO_2^- + O_3 \rightarrow IO_3^- + O_2 \quad \text{(R10)}$$

In this scheme, Reaction (R8) is rate-limiting ($k_8 \sim 1 \times 10^{-12}$ cm^3 molecule^{-1} s^{-1}; Bhujel et al., 2020), whereas the further steps (Reactions R9–R10) in the sequential oxidation to iodate proceed with rate constants at least 2 orders of magnitude larger (Teiwes et al., 2018; Bhujel et al., 2020). IO^- and IO_2^- also react with O_2 to reform O_3:

$$IO^- + O_2 \rightarrow I^- + O_3 \quad \text{(R11)}$$
$$IO_2^- + O_2 \rightarrow IO^- + O_3, \quad \text{(R12)}$$

with rate coefficients of $k_{11} = 3.2 \times 10^{-14}$ cm^3 molecule^{-1} s^{-1} and $k_{12} = 1.3 \times 10^{-14}$ cm^3 molecule^{-1} s^{-1} (Bhujel et al., 2020). With the O_3 ($\sim$ 1–5 $\times 10^{10}$ molecule cm^{-3}), O_2 concentrations ($\sim 4\times$ that of O_3) and reaction times used in their studies (Teiwes et al., 2018, 2019; Bhujel et al., 2020), IO_3^- was observed to be the dominant form of IO_x^-.

In the presence of water vapour, I^- is also present as a hydrate $I^-(H_2O)$ (see above) for which, according to Teiwes et al. (2019), the rate coefficient for reaction with O_3 (Reactions R13a, R13b) is a factor ~ 40 larger than k_8 and results in the formation of IO_2^- and I^-:

$$I^-(H_2O) + O_3 \rightarrow IO_2^- + \text{neutrals} \quad \text{(R13a)}$$
$$I^-(H_2O) + O_3 \rightarrow I^- + \text{neutrals}. \quad \text{(R13b)}$$

As Reaction (R8) is rate-limiting, this implies an increase in the amount of, for example, IO_3^- formed in the IMR in the presence of water. In most regions of the troposphere and lower atmosphere, ozone mixing ratios lie between 30 and $>$ 1000 ppbv. An ambient ozone concentration of 50 ppbv results in a concentration in the IMR of $> 10^{10}$ molecules cm^{-3}. The large rate coefficients for Reactions (R9) and (R10) and the reactions of IO^- and IO_2^- with O_2 result in the rapid inter-conversion of I^-, IO^-, IO_2^- and IO_3^-, which results (for a given RH and ozone concentration) in a quasi-equilibrium between IO_x^- anions.

We explored the relevance of these reactions for our I-CIMS by carrying out a set of experiments in which varying amounts of O_3 were added to the inlet and the mass-to-charge ratios corresponding to IO^- (m/z 143), IO_2^- (m/z 159) and IO_3^- (m/z 175) were monitored; the results are depicted in Fig. 3.

First, we note that all three mass-to-charge ratios were indeed observed, but only under conditions where the CDC potential was set to the lowest value at which ions still reach the detector. The dependence of the various IO_x^- anions on the O_3 mixing ratio is broadly as expected from the reaction scheme (Reactions R8–R12) listed above: the major contributor to IO_x^- at low [O_3] is IO^-, which is converted to IO_2^- and IO_3^- more efficiently as O_3 increases, while the total concentration of IO_x^- increases approximately linearly. At the maximum O_3 mixing ratio used (577 ppbv) there is (following dilution) 375 ppbv in the IMR, which translates to a concentration (at 24 mbar and $\sim$ 298 K) of 2.1×10^{11} molecule cm^{-3}. This O_3 concentration is comparable with those used by Teiwes et al. (2018) ($\sim$ 1–4 $\times 10^{11}$ molecule cm^{-3}) or Bhujel et al. (2020) ($\sim 4 \times 10^{10}$ molecule cm^{-3}) in their ion-trap-based, kinetic investigations of the formation of IO_x^- when reacting I^- with O_3. Their observation that IO_3^- is the dominant anion is however not consistent with our results, which indicate that IO_3^- represents only $\sim$ 35 % of the total IO_x^- signal. The relative abundance of each IO_x^- depends not only on the O_3 concentration but also on the reaction time, which, for both Teiwes et al. (2018) and Bhujel et al. (2020) was between 10–100 ms. Based on the flow into the IMR, its volume ($\sim$ 50 cm^3) and the pressure, we calculate a similar residence time (for neutrals) of about 25 ms. We also considered the possibility that the application in our I-CIMS of a potential difference between the entrance and exit of the IMR (to optimise ion transmission) could result in a significantly shorter IMR residence time for ions. This was assessed by calculating the drift velocity (V_d) in the IMR from the electric field strength ($E \sim 12$ V m^{-1}) and the ion mobility (μ).

$$V_d = E\mu \quad (1)$$

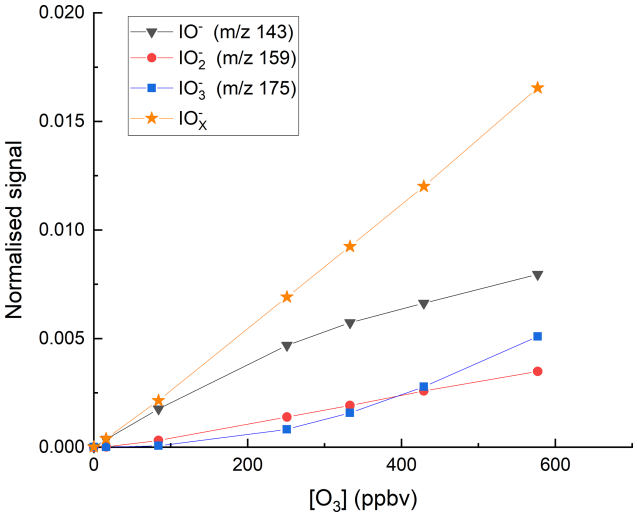

Figure 3. Variation of the I-CIMS signals at m/z 143 (IO^-), 159 (IO_2^-) and 175 (IO_3^-) with the mixing ratios of O_3. The O_3 mixing ratios are those measured in air before the gas flow entered the inlet. The water vapour was held constant using our standard setting ($[H_2O]_{IMR} = 2.9 \times 10^{14}$ molecule cm^{-3}).

The electrical mobility of I^- was calculated for our conditions (using the Mason–Schamp equation) as $\sim 0.15\,m^2\,V^{-1}\,s^{-1}$ using a collision cross-section (for an I^-/N_2 pair) of $9\times10^{-16}cm^2\,molecule^{-1}$ (McCracken, 1952). Via Eq. (1), this results in a drift velocity of $1.8\,m\,s^{-1}$, or an ion residence time (in the ~ 8 cm long IMR) of 44 ms, which is comparable to the residence time of neutrals. Note that the IMR reaction times we derive are only approximate as we do not take into account the mixing and flow dynamics in the IMR, which are likely to be complex (and possibly shorter than 25 ms) owing to sampling via a critical orifice. While we cannot rule out that our observation of IO^- (and not IO_3^-) being the dominant ion signal is partially caused by differences in reaction times, slight differences in O_3 concentrations and differences in temperature (our IMR is at ~ 15 °C above ambient temperature owing to the heated inlet), we note that the higher pressure of O_2 (factor ~ 1–10×10^4) in our IMR is likely to have a large effect. The presence of O_2 converts IO_3^- back to IO^-, thus competing with further oxidation (via reaction with O_3) to IO_3^-. Additionally, the high IMR pressures (24 mbar) in our experiments are ~ 6 orders of magnitude higher than the $\sim 10^{-5}$ mbar available in the ion-trap experiments of Teiwes et al. (2018) and Bhujel et al. (2020), which will result in more rapid thermalisation of the ions present and prevent potentially non-thermal reactions and thus bias to the rate coefficients derived.

The effect of adding H_2O to the IMR was explored in a further set of experiments, and the variations of the signals at mass-to-charge ratios corresponding to IO_x^- with $[H_2O]$ are displayed in Fig. 4. The experiments were carried out with the O_3 mixing ratio fixed at either 70 or 120 ppbv, close to that typically found in the lower troposphere ($\sim$ 20–100 ppbv). At the lowest H_2O concentrations in our experiments, the total IO_x^- signal is about 30 counts. This increases by a factor of ~ 10 when $[H_2O]_{IMR}$ increases to 3×10^{15} molecule cm^{-3}. Increasing the O_3 mixing ratio from 70 to 120 ppbv results in an increase in the signals at m/z 175 (IO_3^-) and m/z 159 (IO_2^-) at all water vapour concentrations, whereas the signal at m/z 143 (IO^-) is reduced at the lowest water vapour concentrations. These observations reinforce the concept of a larger rate coefficient for reaction of $I^-(H_2O)$ with O_3 (Reaction R13a) compared to I^- (Reaction R8) (Teiwes et al., 2019) and the sequential conversion of IO^- to more oxidised forms as described by Reactions (R8)–(R10).

Having established that all of the expected IO_x^- anions are present in our IMR, we can propose a route for HNO_3 detection as NO_3^-, which involves transfer of a proton from HNO_3 (a very strong acid) to the conjugate base of the respective iodine containing acids (hypoiodous, iodous and iodic acid):

$$IO^- + HNO_3 \rightarrow NO_3^- + HOI \quad \text{(R14)}$$

$$IO_2^- + HNO_3 \rightarrow NO_3^- + HOIO \quad \text{(R15)}$$

$$IO_3^- + HNO_3 \rightarrow NO_3^- + HOIO_2. \quad \text{(R16)}$$

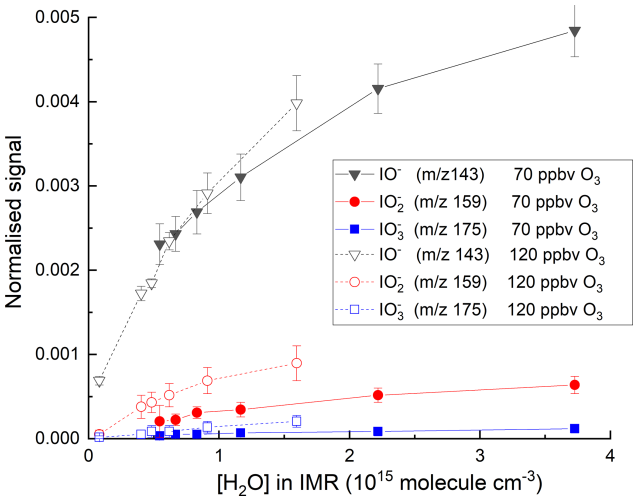

Figure 4. Variation in the total ion signal (counts) due to IO^-, IO_2^- and IO_3^- with the concentration of water vapour in the IMR. The results are from two sets of experiments where the O_3 mixing ratio was either 70 or 120 ppbv.

Taking IO_3^- as an example, we see that the net reaction, $(I^- + O_3 + HNO_3 \rightarrow NO_3^- + HOIO_2)$ is driven by the relative stability of iodic acid compared to O_3, thus bypassing the thermodynamic barrier to direct formation of NO_3^- from $HNO_3 + I^-$. Using heats of formation (in kJ mol^{-1} at 298 K) of $\Delta H_f(IO_3^-) = -211$ (Eger et al., 2019), $\Delta H_f(HNO_3) = -134$ (Goos et al., 2005), $\Delta H_f(HOIO_2) = -95$ (Khanniche et al., 2016) and $\Delta H_f(NO_3^-) = -312$ (Goos et al., 2005), we calculate that Reaction (R16) is exothermic by $\sim 62\,kJ\,mol^{-1}$.

As described above, the O_3 dependence of the ion signals we observe for IO^-, IO_2^- and IO_3^- is consistent with the sequential oxidation of I^- by O_3. However, the relative ion abundance we observe at the detector does not necessarily reflect the relative concentration of the ions in the IMR, and we cannot assign the individual contribution of any single IO_x^- anion to HNO_3 detection. We are unable to completely shut of collisional dissociation in our I-CIMS, which may be a characteristic that is peculiar to our instrument as we do not detect weakly bound I^-(R(O)OH) clusters which are commonly monitored in other instruments utilising I^- chemical ionisation (Lee et al., 2014). Hence, our relative sensitivity to the IO_x^- components is unknown.

In order to confirm that IO_x^- is responsible for detection of HNO_3, we examined the depletion of the signals at m/z 143, m/z 159 and m/z 175 when adding very large concentrations of HNO_3 to the IMR. The results, summarised in Fig. 5, indicate that all three IO_x^- ions are removed when the HNO_3 mixing ratio was increased from zero to 80 ppbv, but with different fractional changes. This can be understood if, for example, the individual IO_x^- reacts with HNO_3 with different rate coefficients. The solid lines in Fig. 5 represent exponential decays of each ion, with rate coefficients

of $\sim 10 \times 10^{-10}$ cm^3 molecule^{-1} s^{-1} for $HNO_3 + IO_3^-$, $\sim 7 \times 10^{-10}$ cm^3 molecule^{-1} s^{-1} for $HNO_3 + IO_2^-$ and $\sim 3 \times 10^{-10}$ cm^3 molecule^{-1} s^{-1} for $HNO_3 + IO^-$. These approximate values were derived by converting the HNO_3 mixing ratio into a concentration in the IMR and assuming pseudo-first-order behaviour (i.e. negligible depletion of HNO_3) so that (using IO_3^- as example)

$$S(IO_3^-)_t = S(IO_3^-)_0 \exp(-kt[HNO_3]_{IMR}),$$

where $S(IO_3^-)_t$ and $S(IO_3^-)_0$ are the signals at m/z 175 after and prior to addition of HNO_3, respectively. $[HNO_3]_{IMR}$ is the concentration (molecule cm^{-3}) of HNO_3 in the IMR, k (cm^3 molecule^{-1} s^{-1}) is the rate coefficient for reaction between HNO_3 and IO_3^-, and t is the reaction time, which we assume to be 25 ms (see above). This analysis assumes that the re-establishment of equilibria between IO_x^- is minimal on the timescale of the reaction between any single IO_x^- and HNO_3. The results indicate qualitatively that IO_3^- is the most reactive of the IO_x^- anions towards HNO_3 but that all three contribute to HNO_3 detection. The depletion of the summed IO_x^- signals versus the accompanying increase in signal due to NO_3^- at m/z 62 is displayed in Fig. 6, which indicates a roughly linear relationship, confirming that IO_x^- is mainly responsible for detection of HNO_3 in our I-CIMS. We note that the absolute increase in signal at m/z 62 is about a factor of 100 greater than the reduction in the signal from IO_x^-, implying that the detection of IO_3^- in our instrument is inefficient.

While the reactions of IO_x^- with HNO_3 represent the most likely route to HNO_3 detection at m/z 62 in our CIMS, other possibilities are the reactions of oxide, superoxide and ozone anions (O_x^-) and hydrated O_x^- with HNO_3 as they have large rate coefficients ($> 10^{-9}$ cm^3 molecule^{-1} s^{-1}) and form NO_3^- (Huey, 1996; Wincel et al., 1996; Lengyel et al., 2020):

$$O^- + HNO_3 \rightarrow NO_3^- + OH \quad \text{(R17)}$$

$$O_2^- + HNO_3 \rightarrow NO_3^- + HO_2 \quad \text{(R18)}$$

$$O_3^- + HNO_3 \rightarrow NO_3^- + \text{neutrals.} \quad \text{(R19)}$$

However, when adding O_3 (up to 600 ppbv) to the IMR, we saw no signal that could be attributable to any oxide anion O_x^-.

Figure 7a displays the dependence of the NO_3^- signal at m/z 62 on the O_3 mixing ratio with HNO_3 held constant at 40($\pm$6) ppbv. The dependence of the normalised signal at m/z 62 on $[O_3]$ is clearly non-linear. We showed above that the sum of all IO_x^- anions increases approximately linearly with O_3 mixing ratio while at the same time the behaviour of IO^- and IO_3^- is more complex. The sensitivity of HNO_3 detection to changes in O_3 concentration is expected to depend not only on the individual concentrations of each anion in the IMR but also on their respective rate coefficients for reaction with HNO_3 (which are different, see above), and

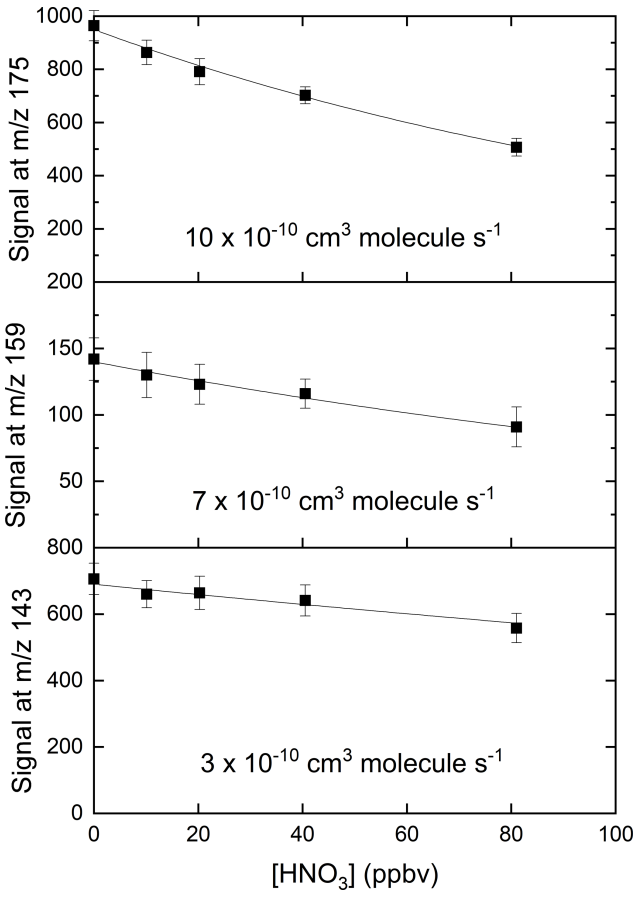

Figure 5. Relative changes in signals at m/z 143 (IO^-), m/z 159 (IO_2^-) and m/z 175 (IO_3^-) when adding up to 80 ppbv of HNO_3. The rate coefficients were calculated using a reaction time of 25 ms and should thus only be regarded as approximate.

the observed non-linearity is not surprising. The solid lines through the data points are regressions of the form

$$\text{signal } (m/z\ 62) = A(1 - \exp(-[O_3]B)), \quad (2)$$

which reflects the expected, approximately exponential dependence of the concentration of IO_x^- in the IMR on the O_3 concentration. In Eq. (2), $[O_3]$ is the O_3 mixing ratio in ppbv and B has a value of 1.515×10^{-3} per ppbv of O_3. As shown in Fig. 7b, for a given $[HNO_3]$, the parameter A is dependent on the water vapour concentration (i.e. on ratio of signals at m/z 145 and m/z 127, (S_{145}/S_{127})) over the range explored and can be parameterised as

$$A = 0.138 + 0.929 \times (S_{145}/S_{127}). \quad (3)$$

In these experiments, H_2O was not added to the thermal dissociation (TD) inlet (this would have increased the retention time of HNO_3 on inlet surfaces, thereby making changes in the m/z 62 difficult to interpret) but directly to the IMR, as described in Sect. 2 and as used during airborne operation of the CIMS. The linear dependence of the signal at m/z 62

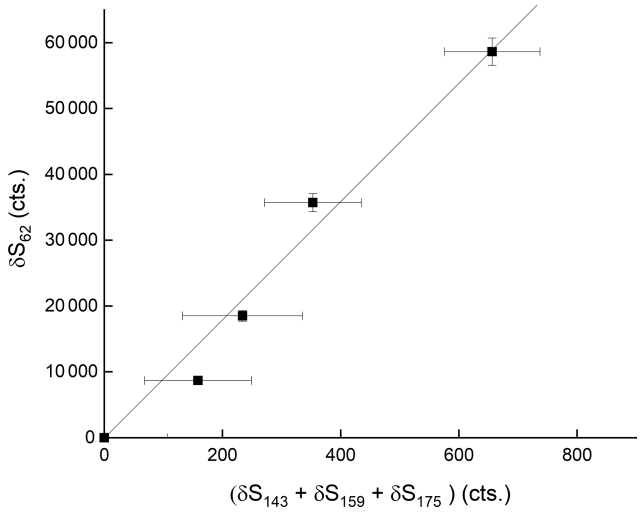

Figure 6. Relative changes in the sum of signals at m/z 143 (IO^-), m/z 159 (IO_2^-) and m/z 175 (IO_3^-) when adding up to 80 ppbv of HNO_3. δ refers to the change in signal upon adding HNO_3 and thus takes background signals at each mass-to-charge ratio into account.

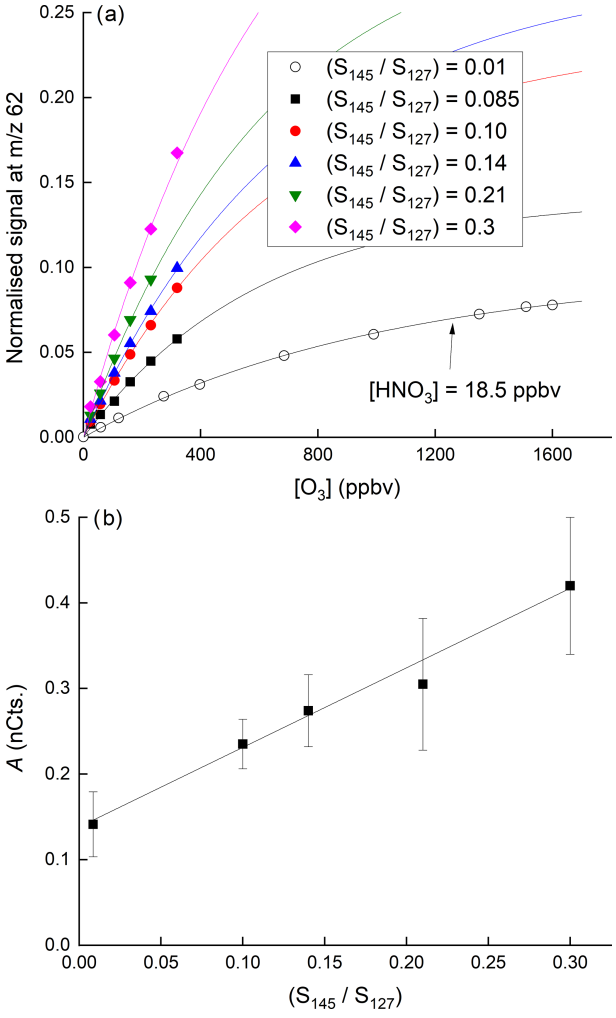

Figure 7. (a) Dependence of the signal at m/z 62 on the O_3 mixing ratio for six different concentrations of H_2O in the IMR. In the upper five curves (solid symbols) the HNO_3 mixing ratio was 38.5 ppbv. In the lowermost curve, the HNO_3 mixing ratio was 18.5 ppbv, as indicated. The fits lines are of the following form: $y = A*\exp(1-\exp(-B*[O_3]))$. **(b)** Plot of parameter A versus the relative signal at m/z 145 and m/z 127.

on the ratio of signals at m/z 145 and m/z 127 at various ozone concentrations ([HNO_3] fixed at 38.5 ppbv) is further highlighted in Fig. S3.

The positive intercept in Fig. 7b indicates that there is significant sensitivity to HNO_3 detection at m/z 62 in the absence of water in the IMR, implying that IO_x^- anions can react directly with HNO_3 to form NO_3^- as written in Reactions (R14)–(R16). The increase in the sensitivity to HNO_3 as the water vapour concentration is increased is consistent with the formation of $I^-(H_2O)$ (m/z 145) which reacts more rapidly with O_3 (to form IO_2^- directly) than does I^- (Teiwes et al., 2019), thereby increasing the abundance of IO_x^- in the IMR (see above) and thus the instrument's sensitivity to HNO_3.

The very strong sensitising effect of ozone and H_2O vapour can explain why similar instruments to ours observe large signals at m/z 62 when sampling ambient air. Indeed, both O_3 and HNO_3 are ubiquitous and generally present at much higher levels than either NO_3 or N_2O_5. Attempts to measure these traces gases using I-CIMS without TD inlets and NO titration (to remove the HNO_3 contribution) will likely result in erroneously high levels of both, especially during the day when lower-tropospheric O_3 and HNO_3 are often at their highest levels. It also explains why laboratory tests (generally carried out without added O_3 or H_2O) have shown only low (or no) sensitivity to HNO_3 at m/z 62.

3.2 Detection of HNO_3 at m/z 190

We now compare the detection of HNO_3 at m/z 62 to its detection at m/z 190, the $I^-(HNO_3)$ adduct, with various amounts of O_3 present. In Fig. 8 we present the results of an experiment in which a constant flow of HNO_3 (12.5 ppbv) was introduced into the inlet and the ozone mixing ratio was varied from zero to 900 ppbv. We observe a great increase in the signal at m/z 62 as expected (from 9 counts to $>$ 6000 counts). At zero ozone, the signal at m/z 190 is about 1000 counts and is largely background free, making this the preferred mass to monitor HNO_3 in the absence of O_3. The cross-over point (when the signals at m/z 62 and m/z 190 are equal) is at an ozone mixing ratio of 100 ppbv. At an ozone mixing ratio of 800 ppbv, the signal at m/z 62 is a factor 8.5 larger than that at m/z 190.

Apparent from this figure is the depletion of the signal at m/z 190 as the O_3 mixing ratio increases to values of 800 ppbv, as present, for example, in the lower stratosphere. The solid lines are least-squares fits to the datasets that de-

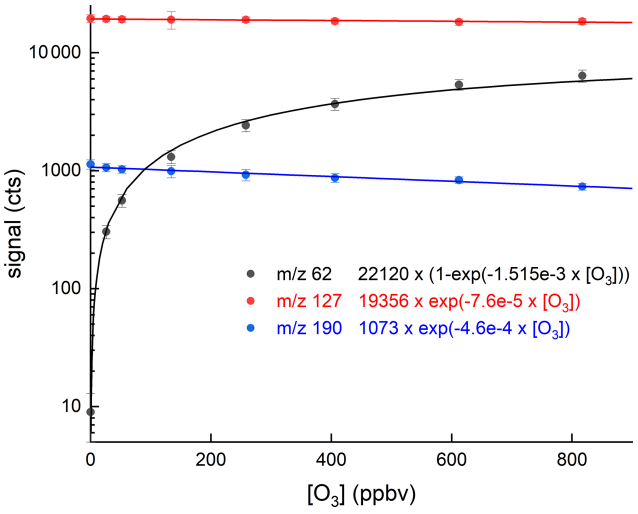

Figure 8. Dependence of the signals at m/z 62 and m/z 190 on the O_3 mixing ratio with HNO_3 fixed at 12.5 ppbv. The lines through the data are described by the expressions listed in the figure.

scribe the exponential growth of the m/z 62 signal as O_3 is increased and the exponential decay of m/z 190 over the same range. The reduction in signal at m/z 190 is characterised by an exponential term $\exp(-0.00046 \times [O_3])$, which means that at 800 ppbv O_3 a $\sim 30\,\%$ reduction in sensitivity is observed. The loss of sensitivity at m/z 190 is driven by the loss of I^- in the IMR as O_3 is added. At the same time, the depletion of the signal at m/z 127 is weaker, which reflects the fact that only a small fraction of IO_x^- formed in the IMR are detected, the rest presumably being fragmented in the CDC before being detected as I^-.

The fact that some I^- is converted to IO_x in the IMR at high O_3 levels but is not reflected in the I^- signal at m/z 127 has repercussions for normalisation of product ion signals to the primary ion signal whereby the assumption is made that the measured signal at m/z 127 stems only from I^-. In our instrument, the loss of I^- in the IMR is significant at high levels of O_3 (e.g. 30 % at 800 ppbv O_3). For this reason, we normalise the signals using values of the signal at m/z 127 obtained by interpolating between measurements obtained when scrubbing the air. The normalisation problem may occur in other I-CIMS instruments to varying extents, and the degree of bias will depend on the conversion of I^- to IO_x^- and the extent to which IO_x^- is detected as I^-. The potential bias can be circumvented by the continuous addition of a calibration gas that is detected via reaction with I^-.

3.3 Detection of HNO_3 at m/z 62: the role of acetate anions

We have also evaluated the potential for "unintentional" HNO_3 detection at m/z 62 by its reaction with the acetate anion, $CH_3CO_2^-$:

$$CH_3CO_2^- + HNO_3 \rightarrow NO_3^- + CH_3C(O)OH. \quad \text{(R20)}$$

The $CH_3CO_2^-$ anion is the conjugate base of a weak acid ($CH_3C(O)OH$) has been utilised to monitor a number of trace gases via proton transfer (Veres et al., 2008). While Veres et al. (2010) generated $CH_3CO_2^-$ deliberately by passing acetic anhydride through their ^{210}Po source, in our experiments it is the product (monitored at m/z 59) of the reaction between I^- primary ions and either $CH_3C(O)O_2$ (from the thermal dissociation of PAN) or $CH_3C(O)OOH$.

$$I^- + CH_3C(O)O_2 \rightarrow CH_3CO_2^- + IO \quad \text{(R21)}$$
$$I^- + CH_3C(O)OOH \rightarrow CH_3CO_2^- + HOI \quad \text{(R22)}$$

Figure 9a shows the result of a set of experiments demonstrating HNO_3 detection at m/z 62 without (blue data points) and with 3.25 ppbv of $CH_3C(O)OOH$ (black data points) added to the inlet flow. The initial (non-normalised) signal at m/z 59 from the $CH_3CO_2^-$ anion in the absence of HNO_3 was 53 500 counts. The presence of 3.25 ppbv $CH_3C(O)OOH$ (and resultant $CH_3CO_2^-$) results in a $\sim$ 50-fold increase in the sensitivity of the I-CIMS to HNO_3. We also carried out a few experiments (less systematic) in which PAN (instead of PAA) was added to the IMR and obtained the same results.

Our results disagree with the conclusions of Wang et al. (2014), who saw no increase at m/z 62 when adding PAN to air containing HNO_3 but are consistent with the use of $CH_3CO_2^-$ as a primary reactant ion to detect HNO_3 at m/z 62 (Veres et al., 2008). Figure 9b indicates that the increase in signal at m/z 62 when adding HNO_3 to a flow of $CH_3C(O)OOH$ in air is approximately proportional to the reduction in the ion signal at m/z 59. This helps confirm that $CH_3CO_2^-$ is the ion responsible for the detection of HNO_3 but also indicates that the detection of PAN and $CH_3C(O)OOH$ via conversion to $CH_3CO_2^-$ can be compromised when HNO_3 is present in the air sample. Indeed, in many air masses the concentration of HNO_3 can be an order of magnitude greater than that of either PAN or $CH_3C(O)OOH$, and given that other abundant trace gases (e.g. organic acids) also react with $CH_3CO_2^-$ (Veres et al., 2008), further reactions of $CH_3CO_2^-$ in the ion–molecule reactor regions of I-CIMS instruments may result in a significant bias (to lower values) which would have to be analysed case by case for different instruments. One way to avoid this problem is the continuous addition of isotopically labelled PAN to the inlet (see e.g. Roiger et al., 2011) as the secondary, reactive losses of ^{12}C and ^{13}C $CH_3CO_2^-$ are expected to be identical.

Wang et al. (2014) observed that the majority of the m/z 62 signal during the daytime could be removed by addition of NO (0.54 ppmv or 1.3×10^{13} molecule cm^{-3}) to the inlet. At their inlet temperature of 120–180 °C, NO reacts with O_3 with a rate coefficient in the range 6–9 $\times$

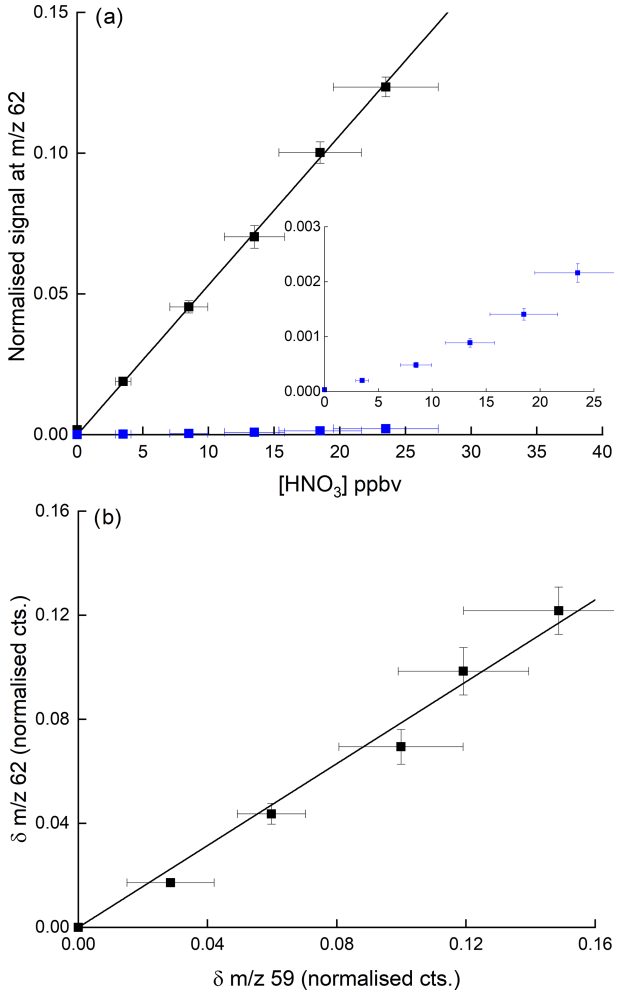

Figure 9. (a) Detection of HNO_3 at m/z 62 in the presence of 3.25 ppbv PAA (and thus the acetate anion, CH_3CO_2). The blue data points (expanded view in the inset) were obtained in the absence of PAA, whereby detection of HNO_3 at m/z 62 is inefficient. The error bars are 1σ statistical uncertainty in the signal at m/z 62 and 17 % total uncertainty in the HNO_3 mixing ratio. **(b)** Change in normalised signals at m/z 62 and m/z 59 upon adding HNO_3 for the same dataset (i.e. background corrected signals). The error bars are 1σ statistical uncertainty.

10^{-14} cm^3 molecule^{-1} s^{-1}, which results in a half-life for O_3 of 500 to 800 ms. Wang et al. (2014) do not mention the residence time of air passing through their heated inlet, but it appears plausible that a substantial fraction of ambient O_3 would have been removed during background measurement, thus decreasing (or removing) sensitivity towards HNO_3 via reactions involving O_3 in the IMR, and leading the authors to conclude that NO_3 was being detected above a lower background than truly present.

To illustrate the potential size of the bias due to HNO_3 when monitoring N_2O_5 at m/z 62 in field measurements, we take the relative sensitivities (at m/z 62) of our I-CIMS to N_2O_5 and to HNO_3 in the presence of typical boundary layer mixing ratios of O_3 (50 ppbv) and at typical relative humidity (50 %). Under these conditions, with N_2O_5 and HNO_3 mixing ratios of 0.2 and 2 ppbv, respectively, we calculate that HNO_3 would account for > 70 % of the signal at m/z 62.

4 Field measurements

Having shown that HNO_3 is detected by our I-CIMS with reasonable sensitivity when sufficient O_3 is present in ambient air samples, we now examine the signals at m/z 62 obtained in airborne operation of the I-CIMS during two CAFE (Chemistry of the Atmosphere Field Experiment) campaigns of the HALO aircraft. In the CAFE-Africa campaign (2018) the I-CIMS monitored m/z 62 on several flights over the Atlantic west of the African continent. During the 2020 CAFE-EU campaign with HALO over Europe, the I-CIMS additionally monitored m/z 190 (the $I^-(HNO_3)$ cluster ion), which is selective to HNO_3. During both campaigns, O_3 and H_2O (required for analysis of the signal at m/z 62) were routinely measured.

4.1 CAFE-Africa

Here we examine the results obtained during a HALO flight as part of the CAFE-Africa mission. The flight in question was the transfer from Sal airport on the Cabo Verde islands (which served as the base station during the mission) back to Germany. During the flight the aircraft flew mainly at high altitudes (13–15 km) so that stratospheric air was sampled at higher latitudes but also made two dives into the free troposphere. The flight track is displayed in Fig. S4.

Figure 10 shows a time series of ozone mixing ratios during the flight (panel a) along with the I-CIMS signal at m/z 62 (panel b). In air masses with stratospheric influence (i.e. O_3 values > 100 ppb, 12:20–15:10 UTC) there is an obvious, strong co-variance between these two parameters. However, once corrected for the dependence of the sensitivity of the I-CIMS to O_3 (Eqs. 2 and 3) we obtain the black line representing the mixing ratios of HNO_3 and the covariance is greatly reduced. We also note that, apart from some significant increases at ∼ 11:30 and ∼ 16:00, the HNO_3 mixing ratio decreases slowly throughout the flight, which is the result of HNO_3 generation in the ^{210}Po source leading to an initially large background signal. The formation of HNO_3 in the ^{210}Po source has been documented previously (Ji et al., 2020); its level can be reduced by permanently flushing N_2 through the source while keeping the mass spectrometer under operational vacuum. This was not carried out during the CAFE missions on HALO as continuous operation of the instrument (i.e. overnight between flights) was not possible. We note that the background signal at m/z 62 that originates from the polonium source cannot be obtained by scrubbing the air of HNO_3 as this also removes O_3 and thus also sensitivity to HNO_3 at this mass.

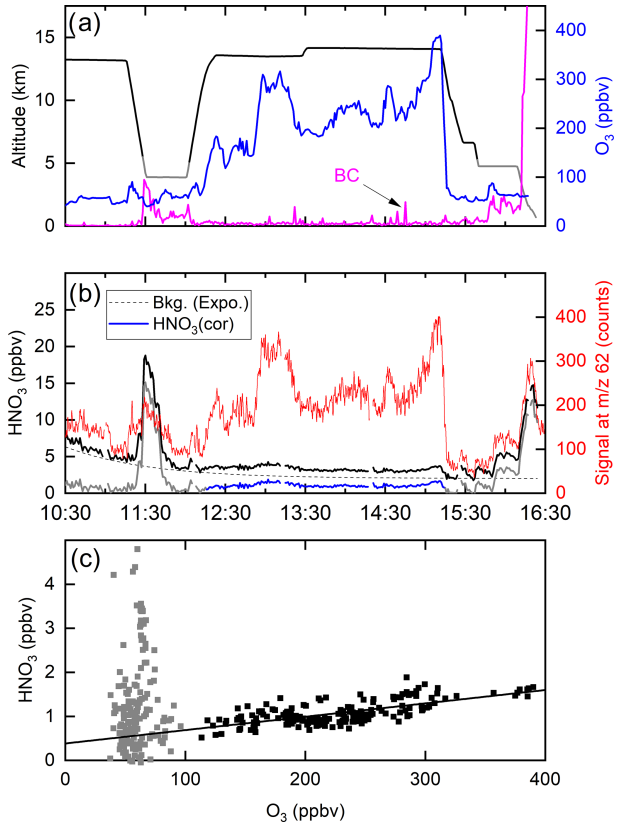

Figure 10. **(a)** Altitude (black) and O_3 mixing ratios (blue) from a HALO flight during the CAFE-Africa campaign. The purple line (arbitrary units) is proportional to the black-carbon particle number density (BC). **(b)** The signal at m/z 62 (red line) clearly co-varies with O_3. Following conversion to a mixing ratio (black line) and subtraction of an HNO_3 background signal (dotted line, assuming an exponential decay) originating in the ^{210}Po source, the solid blue line for HNO_3 is obtained (HNO_3 cor). **(c)** HNO_3 mixing ratios plotted versus O_3 mixing ratios. The straight black line has a slope of $(3 \pm 0.5) \times 10^{-3}$ and does not take into account the grey data points (O_3 mixing ratio < 100 ppbv).

A roughly exponential decay of the HNO_3 background signal was observed in all of the flights in which m/z 62 was monitored, which presumably reflects depletion of the initially large HNO_3 reservoir which was built up when the I-CIMS was switched off.

A coarse correction of the dataset was thus undertaken by subtracting an exponentially decaying background from the total HNO_3 signal. The resulting HNO_3 mixing ratios are depicted as the blue line in Fig. 10b and plotted against the O_3 mixing ratio in Fig. 10c. Considering only the high-altitude data for which O_3 mixing ratios were > 100 ppbv (stratospheric influence, black data points), we derive a slope of $HNO_3/O_3 = (3 \pm 0.5) \times 10^{-3}$ (the uncertainty is 2σ, statistical only), which is consistent with previously reported values obtained in airborne measurements of HNO_3 and O_3 in the lower stratosphere (see Popp et al., 2009, and references therein). We stress that deriving accurate mixing ratios of HNO_3 is not possible with this dataset, and the values obtained are strongly dependent on the background correction. Here, we merely wish to indicate that, while most of the variability in our m/z 62 signal is related to the central role of ozone in the detection scheme (i.e. formation of IO_x^-), some covariance between HNO_3 and O_3 remains after correction of the raw data and the slope is roughly in line with that expected. We also do not propose that the correlation of m/z 62 with O_3 proves that the signal can be attributed entirely to HNO_3. This aspect will be covered in Sect. 4.2.

Figure 10b reveals sharp increases in the (background-corrected) HNO_3 mixing ratio when sampling at lower altitudes, noticeably at 11:30–12:00 (3.9 km altitude) and at 15:45–16:10 (4.7 km altitude) and at the end of the flight during descent to Oberpfaffenhofen in Bavaria, Germany. In all cases, these periods of enhanced HNO_3 coincided with higher levels of particles. Back trajectories (HYSPLIT) indicated that, in the 10 d prior to interception by HALO, the air mass sampled at 11:30 had passed over the West African continent (Mauritania, Mali and Niger), whereas the air masses sampled after 16:00 were of European origin. The large, coincidental increase in the HNO_3 mixing ratio and particle mass was a recurrent feature of the CAFE-Africa flights. It is conceivable that the HNO_3 measured by the I-CIMS was a mixture of gas-phase HNO_3 and HNO_3 associated with particles that desorb HNO_3 when passing through the thermal dissociation inlet at 180 °C. This temperature would be sufficient to thermally convert ammonium nitrate to HNO_3 (and NH_3) as well as to result in the desorption of HNO_3 that was physisorbed, for example, on chemically aged black-carbon or mineral-dust particles. As we do not know the efficiency with which particles of various diameters enter the TD inlet of the CIMS, we cannot estimate the relative contribution of gas-phase and particulate nitrate to the signal at m/z 62 but indicate that a similar phenomenon may occur in ground-based measurements using TD inlets and may represent an additional source of bias during ambient measurements of NO_3 and/or N_2O_5 at m/z 62.

4.2 CAFE-EU

During the CAFE-EU HALO flights the I-CIMS monitored m/z 190, the $I^-(HNO_3)$ adduct, as well as NO_3^- at m/z 62. The detection of HNO_3 at m/z 190 varies with the water vapour concentration in the IMR: the response of the HNO_3 signal at m/z 190 to changes in the HNO_3 concentration and in the m/z 145 : m/z 127 ratio (i.e. the relative humidity in the IMR, see Fig. S2) is illustrated in Fig. S5.

Figure 11 displays a set of data obtained during a flight on 30 May 2020 on which the HALO aircraft flew a path from southern Germany to the Atlantic (west of Ireland) and back at various altitudes (for flight track see Fig. S6). Figure 11a plots the raw signals measured by the I-CIMS at m/z 62 and m/z 190 as well as the O_3 mixing ratio. Similar to the CAFE-

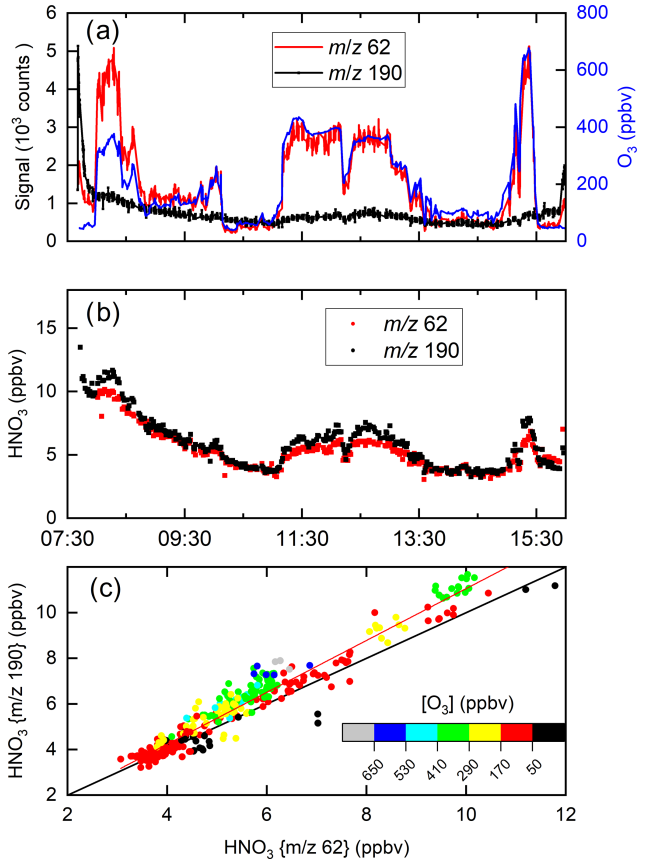

Figure 11. I-CIMS HNO_3 measurements and auxiliary data from a HALO flight during the CAFE-EU campaign. **(a)** Signals at m/z 62 and m/z 190 as well as O_3 mixing ratios. **(b)** HNO_3 mixing ratios derived from the signals at m/z 62 and m/z 190 taking the dependence of sensitivity on ozone and relative humidity into account. **(c)** Correlation of the HNO_3 mixing ratios derived from the two masses. The red line is a bivariate fit (slope 1.14 ± 0.05, intercept -0.3 ± 0.3), and the black line is a 1 : 1 line. A large fraction of the HNO_3 measured stems from the polonium source, especially at the beginning of the flight.

Africa dataset, the signal at m/z 62 covaries strongly with the O_3 mixing ratios, which were between ~ 40 and ~ 700 ppbv, whereas the raw signals at m/z 62 and m/z 190 (both due to HNO_3) bear little resemblance to each other.

Using the calibration parameters described in Sect. 3 and (for m/z 190) in Fig. S3, the signals at m/z 62 and m/z 190 were converted to HNO_3 mixing ratios, depicted in Fig. 11b. Despite the greatly divergent raw signals, the HNO_3 mixing ratios obtained using the different mass-to-charge ratios are in reasonable agreement, both displaying a gradual decrease after take-off at $\sim$08:00 UTC. The high initial level of HNO_3 is largely the result of HNO_3 being formed in the ^{210}Po source during overnight instrument shut-down (see Sect. 4.1). The HNO_3 mixing ratios observed at m/z 62 and m/z 190 both increase when the aircraft sampled stratospheric air (11:00 to 13:00 and 15:10 to 15:30 UTC). In Fig. 11c HNO_3 mixing ratios derived at m/z 62 and m/z 190 are plotted in a correlation diagram. The slope (1.14 ± 0.05) and intercept (-0.3 ± 0.3) indicate reasonable agreement even when the raw signals are greatly divergent at high levels of O_3. At the highest levels of O_3, some differences in the retrieved mixing ratios of HNO_3 using m/z 62 and m/z 190 are observed, which, given the large, O_3-dependent corrections applied (especially for m/z 62), is not surprising. Our airborne data show that in many (if not most) air masses, m/z 62 provides a measure of HNO_3 rather than NO_3 and N_2O_5.

5 Conclusions

A series of laboratory experiments investigating the origin of signal at m/z 62 when using an I-CIMS has revealed unexpected sensitivity to HNO_3 at this mass-to-charge ratio in the presence of O_3 or peroxyacetic acid (PAA) or PAN. The ozone effect is related to the formation of IO_x^-, which reacts rapidly with HNO_3 to form NO_3^- thus bypassing the thermodynamic barrier to formation of NO_3^- by direct reaction of HNO_3 with I^-. The presence of O_3 at a mixing ratio of 500 ppbv results in a 250-fold increase in sensitivity to HNO_3 at m/z 62. The sensitivity to HNO_3 at this mass-to-charge ratio was also found to be highly dependent on the concentration of H_2O in the ion–molecule reactor as this aids formation of IO_x^-. The sensitivity to HNO_3 at m/z 62 in the presence of PAA is a result of the presence of acetate anions ($CH_3CO_2^-$) as demonstrated previously (Veres et al., 2008). We conclude that measurements of PAN using I-CIMS may be biased to low values if large mixing ratios of HNO_3 (or organic acids) are present and continuous calibration (e.g. with isotopically labelled PAN) is not carried out. Our laboratory experiments indicate that measurements of atmospheric NO_3 and N_2O_5 at m/z 62 can be heavily biased by the presence of HNO_3 and may explain reports of unexpectedly high daytime mixing ratios of N_2O_5. The relative sensitivity at m/z 62 to HNO_3 and N_2O_5/NO_3 will vary from one I-CIMS instrument to the next and must thus be analysed case by case.

We have examined signals at m/z 62 during two periods of operation of the I-CIMS on the HALO aircraft: one over the Atlantic west of the African coast and one over Europe. During the flights over Europe HNO_3 mixing ratios derived from m/z 62 NO_3^- and at m/z 190 ($I^-(HNO_3)$) were in good agreement. The data obtained over the Atlantic indicated that measurements at m/z 62 using a thermal dissociation inlet can be strongly influenced by particulate nitrate that can thermally dissociate (or desorb) to gas-phase HNO_3.

Data availability. Data measured during the flight campaign CAFE campaigns are available to all scientists agreeing to the CAFE data protocol. The laboratory data underlying the figures are available upon request to the authors.

Supplement. The supplement related to this article is available online at: https://doi.org/10.5194/amt-14-5319-2021-supplement.

Author contributions. RD conducted the laboratory experiments, carried out the airborne measurements with assistance from PE and JNC, and analysed the laboratory data with assistance from JNC. The manuscript was written by JNC and RD with contributions from all other authors. JL designed and helped plan the airborne operations.

Competing interests. The authors declare that they have no conflict of interest.

Disclaimer. Publisher's note: Copernicus Publications remains neutral with regard to jurisdictional claims in published maps and institutional affiliations.

Acknowledgements. We acknowledge the collaboration with the DLR (German Aerospace Centre) during the HALO campaigns CAFE-Africa and CAFE-EU. We thank Florian Obersteiner and Andreas Zahn (KIT-Karlsruhe) for use of the O_3 data during CAFE-Africa and CAFE-EU.

Financial support. The article processing charges for this open-access publication were covered by the Max Planck Society.

Review statement. This paper was edited by Fred Stroh and reviewed by three anonymous referees.

References

Ammann, M., Cox, R. A., Crowley, J. N., Herrmann, H., Jenkin, M. E., McNeill, V. F., Mellouki, A., Rossi, M. J., Troe, J., and Wallington, T. J.: Atmospheric Chemical Kinetic Data Evaluation, available at: http://iupac.pole-ether.fr/index.html, last access: 20 July 2021.

Atkinson, R., Baulch, D. L., Cox, R. A., Crowley, J. N., Hampson, R. F., Hynes, R. G., Jenkin, M. E., Rossi, M. J., and Troe, J.: Evaluated kinetic and photochemical data for atmospheric chemistry: Volume I – gas phase reactions of O_x, HO_x, NO_x and SO_x species, Atmos. Chem. Phys., 4, 1461–1738, https://doi.org/10.5194/acp-4-1461-2004, 2004.

Bhujel, M., Marshall, D. L., Maccarone, A. T., McKinnon, B. I., Trevitt, A. J., da Silva, G., Blanksby, S. J., and Poad, B. L. J.: Gas phase reactions of iodide and bromide anions with ozone: evidence for stepwise and reversible reactions, Phys. Chem. Chem. Phys., 22, 9982–9989, https://doi.org/10.1039/d0cp01498b, 2020.

Chang, W. L., Bhave, P. V., Brown, S. S., Riemer, N., Stutz, J., and Dabdub, D.: Heterogeneous atmosperic chemistry, ambient measurements and model calculatuons of N_2O_5: A review, Aerosol Sci. Tech., 45, 655–685, https://doi.org/10.1080/02786826.2010.551672, 2011.

Crowley, J. N., Ammann, M., Cox, R. A., Hynes, R. G., Jenkin, M. E., Mellouki, A., Rossi, M. J., Troe, J., and Wallington, T. J.: Evaluated kinetic and photochemical data for atmospheric chemistry: Volume V – heterogeneous reactions on solid substrates, Atmos. Chem. Phys., 10, 9059–9223, https://doi.org/10.5194/acp-10-9059-2010, 2010.

Davidson, J. A., Viggiano, A. A., Howard, C. J., Dotan, I., Fehsenfeld, F. C., Albritton, D. L., and Ferguson, E. E.: Rate Constants for Reactions of O_2^+, NO_2^+, NO^+, H_3O^+, CO_3^-, NO_2^-, and Halide Ions with N_2O_5 at 300 K, J. Chem. Phys., 68, 2085–2087, 1978.

Dubé, W. P., Brown, S. S., Osthoff, H. D., Nunley, M. R., Ciciora, S. J., Paris, M. W., McLaughlin, R. J., and Ravishankara, A. R.: Aircraft instrument for simultaneous, in situ measurement of NO_3 and N_2O_5 via pulsed cavity ring-down spectroscopy, Rev. Sci. Instrum., 77, 034101, https://doi.org/10.1063/1.2176058, 2006.

Dulitz, K., Amedro, D., Dillon, T. J., Pozzer, A., and Crowley, J. N.: Temperature-(208–318 K) and pressure-(18–696 Torr) dependent rate coefficients for the reaction between OH and HNO_3, Atmos. Chem. Phys., 18, 2381–2394, https://doi.org/10.5194/acp-18-2381-2018, 2018.

Eger, P. G., Helleis, F., Schuster, G., Phillips, G. J., Lelieveld, J., and Crowley, J. N.: Chemical ionization quadrupole mass spectrometer with an electrical discharge ion source for atmospheric trace gas measurement, Atmos. Meas. Tech., 12, 1935–1954, https://doi.org/10.5194/amt-12-1935-2019, 2019.

Fehsenfeld, F. C., Howard, C. J., and Schmeltekopf, A. L.: Gas phase ion chemistry of HNO_3, J. Chem. Phys., 63, 2835–2841, https://doi.org/10.1063/1.431722, 1975.

Fischer, H., Waibel, A. E., Welling, M., Wienhold, F. G., Zenker, T., Crutzen, P. J., Arnold, F., Burger, V., Schneider, J., Bregman, A., Lelieveld, J., and Siegmund, P. C.: Observations of high concentrations of total reactive nitrogen (NO_y) and nitric acid (HNO_3) in the lower Arctic stratosphere during the stratosphere-troposphere experiment by aircraft measurements (STREAM) II campaign in February 1995, J. Geophys. Res.-Atmos., 102, 23559–23571, https://doi.org/10.1029/97jd02012, 1997.

Goos, E., Burcat, A., and Ruscic, B.: Extended Third Millennium Ideal Gas and Condensed Phase Thermochemical Database for Combustion with Updates from Active Thermochemical Tables: Update of "Third Millennium Ideal Gas and Condensed Phase Thermochemical Database for Combustion with Updates from Active Thermochemical Tables by Alexander Burcat and Branko Ruscic", Aerospace Engineering, and Argonne National Laboratory, Chemistry Division, Rep. ANL 05/20 and TAE 960 Technion-IIT, September 2005.

Hanson, D. R. and Ravishankara, A. R.: The reaction probabilities of $ClONO_2$ and N_2O_5 on polar stratospheric cloud material, J. Geophys. Res., 96, 5081–5090, 1991.

Huey, L. G.: The kinetics of the reactions of Cl^-, O^-, and O_2^- with HNO_3: Implications for measurement of HNO_3 in the atmosphere, Int. J. Mass Spectrom., 153, 145–150, https://doi.org/10.1016/0168-1176(95)04354-3, 1996.

Huey, L. G.: Measurement of trace atmospheric species by chemical ionization mass spectrometry: Speciation of reactive nitrogen and future directions, Mass Spectrom. Rev., 26, 166–184, https://doi.org/10.1002/mas.20118, 2007.

Huey, L. G., Hanson, D. R., and Howard, C. J.: Reactions of SF_6^- and I^- with atmospheric trace gases, J. Phys. Chem., 99, 5001–5008, https://doi.org/10.1021/j100014a021, 1995.

Iyer, S., He, X. C., Hyttinen, N., Kurten, T., and Rissanen, M. P.: Computational and experimental investigation of the detection of HO_2 radical and the products of its reaction with cyclohexene ozonolysis derived RO_2 radicals by an iodide-based chemical ionization mass spectrometer, J. Phys. Chem. A, 121, 6778–6789, https://doi.org/10.1021/acs.jpca.7b01588, 2017.

Ji, Y., Huey, L. G., Tanner, D. J., Lee, Y. R., Veres, P. R., Neuman, J. A., Wang, Y., and Wang, X.: A vacuum ultraviolet ion source (VUV-IS) for iodide–chemical ionization mass spectrometry: a substitute for radioactive ion sources, Atmos. Meas. Tech., 13, 3683–3696, https://doi.org/10.5194/amt-13-3683-2020, 2020.

Kercher, J. P., Riedel, T. P., and Thornton, J. A.: Chlorine activation by N_2O_5: simultaneous, in situ detection of $ClNO_2$ and N_2O_5 by chemical ionization mass spectrometry, Atmos. Meas. Tech., 2, 193–204, https://doi.org/10.5194/amt-2-193-2009, 2009.

Khanniche, S., Louis, F., Cantrel, L., and Černušák, I.: A theoretical study of the microhydration of iodic acid ($HOIO_2$), Comput. Theor. Chem., 1094, 98–107, https://doi.org/10.1016/j.comptc.2016.09.010, 2016.

Lee, B. H., Lopez-Hilfiker, F. D., Mohr, C., Kurten, T., Worsnop, D. R., and Thornton, J. A.: An iodide-adduct high-resolution time-of-flight chemical-ionization mass spectrometer: Application to atmospheric inorganic and organic compounds, Environ. Sci. Technol., 48, 6309–6317, https://doi.org/10.1021/es500362a, 2014.

Lengyel, J., Oncak, M., and Beyer, M. K.: Chemistry of NO_x and HNO_3 molecules with gas-phase hydrated O^- and OH^- ions, Chem.-Eur. J., 26, 7861–7868, https://doi.org/10.1002/chem.202000322, 2020.

Lightfoot, P. D., Cox, R. A., Crowley, J. N., Destriau, M., Hayman, G. D., Jenkin, M. E., Moortgat, G. K., and Zabel, F.: Organic peroxy radicals – kinetics, spectroscopy and tropospheric chemistry, Atmos. Environ. A-Gen., 26, 1805–1961, 1992.

McCracken, F. L.: Total collision cross sections of negative atomic iodine ions in nitrogen and argon, Phys. Rev. 86, 135, https://doi.org/10.1103/PhysRev.86.135, 1952.

Phillips, G. J., Pouvesle, N., Thieser, J., Schuster, G., Axinte, R., Fischer, H., Williams, J., Lelieveld, J., and Crowley, J. N.: Peroxyacetyl nitrate (PAN) and peroxyacetic acid (PAA) measurements by iodide chemical ionisation mass spectrometry: first analysis of results in the boreal forest and implications for the measurement of PAN fluxes, Atmos. Chem. Phys., 13, 1129–1139, https://doi.org/10.5194/acp-13-1129-2013, 2013.

Popp, P. J., Marcy, T. P., Gao, R. S., Watts, L. A., Fahey, D. W., Richard, E. C., Oltmans, S. J., Santee, M. L., Livesey, N. J., Froidevaux, L., Sen, B., Toon, G. C., Walker, K. A., Boone, C. D., and Bernath, P. F.: Stratospheric correlation between nitric acid and ozone, J. Geophys. Res., 114, D03305, https://doi.org/10.1029/2008jd010875, 2009.

Riva, M., Rantala, P., Krechmer, J. E., Peräkylä, O., Zhang, Y., Heikkinen, L., Garmash, O., Yan, C., Kulmala, M., Worsnop, D., and Ehn, M.: Evaluating the performance of five different chemical ionization techniques for detecting gaseous oxygenated organic species, Atmos. Meas. Tech., 12, 2403–2421, https://doi.org/10.5194/amt-12-2403-2019, 2019.

Roiger, A., Aufmhoff, H., Stock, P., Arnold, F., and Schlager, H.: An aircraft-borne chemical ionization – ion trap mass spectrometer (CI-ITMS) for fast PAN and PPN measurements, Atmos. Meas. Tech., 4, 173–188, https://doi.org/10.5194/amt-4-173-2011, 2011.

Slusher, D. L., Huey, L. G., Tanner, D. J., Flocke, F. M., and Roberts, J. M.: A thermal dissociation-chemical ionization mass spectrometry (TD-CIMS) technique for the simultaneous measurement of peroxyacyl nitrates and dinitrogen pentoxide, J. Geophys. Res.-Atmos., 109, D19315, https://doi.org/10.1029/2004JD004670, 2004.

Teiwes, R., Elm, J., Handrup, K., Jensen, E. P., Bilde, M., and Pedersen, H. B.: Atmospheric chemistry of iodine anions: elementary reactions of I^-, IO^-, and IO_2^- with ozone studied in the gas-phase at 300 K using an ion trap, Phys. Chem. Chem. Phys., 20, 28606–28615, https://doi.org/10.1039/c8cp05721d, 2018.

Teiwes, R., Elm, J., Bilde, M., and Pedersen, H. B.: The reaction of hydrated iodide $I(H_2O)^-$ with ozone: a new route to IO_2^- products, Phys. Chem. Chem. Phys., 21, 17546–17554, https://doi.org/10.1039/c9cp01734h, 2019.

Veres, P., Roberts, J. M., Warneke, C., Welsh-Bon, D., Zahniser, M., Herndon, S., Fall, R., and de Gouw, J.: Development of negative-ion proton-transfer chemical-ionization mass spectrometry (NI-PT-CIMS) for the measurement of gas-phase organic acids in the atmosphere, Int. J. Mass Spectrom., 274, 48–55, https://doi.org/10.1016/j.ijms.2008.04.032, 2008.

Veres, P., Gilman, J. B., Roberts, J. M., Kuster, W. C., Warneke, C., Burling, I. R., and de Gouw, J.: Development and validation of a portable gas phase standard generation and calibration system for volatile organic compounds, Atmos. Meas. Tech., 3, 683–691, https://doi.org/10.5194/amt-3-683-2010, 2010.

Wang, X., Wang, T., Yan, C., Tham, Y. J., Xue, L., Xu, Z., and Zha, Q.: Large daytime signals of N_2O_5 and NO_3 inferred at 62 amu in a TD-CIMS: chemical interference or a real atmospheric phenomenon?, Atmos. Meas. Tech., 7, 1–12, https://doi.org/10.5194/amt-7-1-2014, 2014.

Wayne, R. P., Barnes, I., Biggs, P., Burrows, J. P., Canosa-Mas, C. E., Hjorth, J., Le Bras, G., Moortgat, G. K., Perner, D., Poulet, G., Restelli, G., and Sidebottom, H.: The nitrate radical: Physics, chemistry, and the atmosphere, Atmos. Environ. A-Gen., 25A, 1–206, 1991.

Williams, S., Campos, M. F., Midey, A. J., Arnold, S. T., Morris, R. A., and Viggiano, A. A.: Negative ion chemistry of ozone in the gas phase, J. Phys. Chem. A, 106, 997–1003, https://doi.org/10.1021/jp012929r, 2002.

Wincel, H., Mereand, E., and Castleman, A. W.: Gas phase reactions of DNO_3 with $X^-(D_2O)_n$, X = O, OD, O_2, DO_2, and O_3, J. Phys. Chem., 100, 7488–7493, https://doi.org/10.1021/jp953104i, 1996.

Zheng, W., Flocke, F. M., Tyndall, G. S., Swanson, A., Orlando, J. J., Roberts, J. M., Huey, L. G., and Tanner, D. J.: Characterization of a thermal decomposition chemical ionization mass spectrometer for the measurement of peroxy acyl nitrates (PANs) in the atmosphere, Atmos. Chem. Phys., 11, 6529–6547, https://doi.org/10.5194/acp-11-6529-2011, 2011.